Skin-Friction Measurements and Computational Comparison of Swept Shock/Boundary-Layer Interactions

K.-S. Kim,* Y. Lee,* F. S. Alvi,* and G. S. Settles†
Pennsylvania State University, University Park, Pennsylvania 16802
and
C. C. Horstman‡
NASA Ames Research Center, Moffett Field, California 94035

A joint experimental and computational study of skin friction in weak-to-strong swept shock wave/turbulent boundary-layer interactions has been carried out. A planar shock wave is generated by a sharp fin at angles of attack $\alpha = 10$ and 16 deg at $M_\infty = 3$ and 16 and 20 deg at $M_\infty = 4$. Measurements are made using the laser interferometer skin friction (LISF) meter, which optically detects the rate of thinning of an oil film applied to the test surface. The results show a systematic rise in the peak c_f at the rear part of the interaction, where the separated flow attaches. For the strongest case studied, this peak is an order of magnitude higher than the incoming freestream c_f level. Navier-Stokes computations of these flows agree well with the data for moderate interaction strengths, but systematically underpredict the data with increasing interaction strength. Algebraic eddy-viscosity turbulence models produce the best prediction of the measured c_f distributions but still fail for the strongest cases studied. However, in predicting surface streamline angles, a k-ϵ turbulence model with integration to the wall produced the best results.

Nomenclature

c_f = skin-friction coefficient based on incoming freestream conditions
c_h = heat transfer coefficient
M_∞ = incoming freestream Mach number
p_1 = static pressure before shock wave, MPa
p_2 = static pressure after shock wave, MPa
p_0 = stagnation pressure of incoming freestream, MPa
p_w = wall static pressure on flat plate, MPa
R = radial distance measured from the fin leading edge, mm
Re_θ = Reynolds number based on the local, undisturbed boundary-layer momentum thickness
T_{aw} = adiabatic wall temperature, K
T_w = wall temperature, K
T_0 = freestream stagnation temperature, K
x,y,z = orthogonal streamwise, normal, and spanwise coordinates, mm
y^+ = nondimensional turbulent boundary-layer wall coordinate
α = angle made by fin with respect to the incoming freestream direction, deg
β = angle with respect to freestream direction, measured from fin leading edge, deg
δ_0 = incoming freestream boundary-layer thickness, mm
μ_t = turbulent eddy-viscosity, N-s/m²
μ_∞ = dynamic viscosity of incoming freestream, N-s/m²
ν = oil viscosity, cS

τ_w = wall shear stress, Pa
θ_0 = incoming freestream boundary-layer momentum thickness, mm
ϕ = angle of surface skin-friction line with respect to the incoming freestream direction, deg

Subscripts

expt = experimental value
is = inviscid shock
pa = primary attachment
ps = primary separation
ss = secondary separation
ui = upstream influence
∞ = incoming freestream conditions

Introduction

THE interaction of a swept shock wave with a turbulent boundary layer constitutes one of the fundamental problems of modern high-speed fluid dynamics. As a result of the recent resurgence of interest in high-speed flight, these interactions have been the focus of renewed attention, both in experimental and computational fluid dynamics. A detailed survey of such interactions has been carried out by Settles and Dolling.[1] Due to inherent complexity, the computational modeling of such interactions is very difficult and not entirely reliable at present. One of the key tests of the validity of a computational fluid dynamics (CFD) code is its ability to correctly predict such fundamental flow characteristics as the coefficients of heat transfer and skin friction in complex turbulent flows. The computation of such interactions is presently paced by the need for detailed, "benchmark" experiments. However, heat transfer and especially skin friction are difficult to measure with acceptable accuracy for code validation purposes. Furthermore, there are almost no reliable skin-friction data available in high-speed interacting flows.

A recent development, the laser interferometer skin friction (LISF) meter, produces reliable skin-friction data over a wide range of flow situations where traditional skin-friction methods are not practical. The LISF meter was invented by Tanner and Blows,[2] and subsequently refined by Tanner and Kulkarni,[3] Tanner,[4] Monson and Higuchi,[5] Monson,[6,7] Westphal et al.,[8] and Kim and Settles.[9,10] It interferometically

senses the time rate of thinning of an oil film on a polished surface subjected to aerodynamic shear. Under proper conditions, skin friction can be found directly without any reference to the properties of the overlying boundary layers.

The applicability, repeatability, and accuracy of the LISF technique for use in compressible flows have been determined by Kim and Settles[9] through an experimental calibration in the supersonic Mach number range. In terms of accuracy, the LISF data fell 3–6% below the mean of the four calibration standards used, depending upon M_∞. The overall repeatability of the LISF data was within ±8%, which represents 2 standard deviations about the mean.

Following this calibration experiment, Kim and Settles[10] measured skin-friction distributions at $M_\infty = 3$ in fin-generated, swept shock wave/turbulent boundary-layer interactions. Fin shock-generator angles were chosen to be 10 and 16 deg, which produce weak and moderate-strength interactions, respectively, at this Mach number. These experiments revealed that the LISF technique is practical and useful for skin-friction measurements in three-dimensional, interacting compressible flows. Furthermore, it was shown that pressure- and shear-gradient effects on the LISF data were negligible, in stark contrast to the case for most other methods of skin-friction measurement. The skin-friction results at $M_\infty = 3$, first reported in Ref. 10, are briefly restated in the present paper for completeness.

This paper reports the latest results of a program to obtain reliable measurements of skin friction in swept shock wave/boundary-layer interactions. The LISF c_f measurements of Ref. 10 have been extended to include $\alpha = 16$ and 20 deg at $M_\infty = 3.98$. These results are compared with CFD calculations using four different turbulence models. An overall view of both c_f variations and CFD predictive capability for weak-to-strong swept interactions is thus presented.

Experimental Methods

Wind Tunnel Facility and Test Conditions

The experiments were performed in the Supersonic Wind Tunnel Facility of the Penn State Gas Dynamics Laboratory, which has been shown to produce good flow quality over a nominal Mach number range of 1.5–4. The wind tunnel is an intermittent blowdown type, which provides the variable Mach number capability by way of an asymmetric sliding-block nozzle. The test section of the wind tunnel is 152 mm wide, 165 mm high, and 610 mm long. Wind tunnel runs for the present study were of 20–30 s duration.

The test Mach number was fixed at 3.98 ±0.071 in this study. The stagnation conditions of the flow were $p_0 = 1.524$ MPa ±2.4% and $T_0 = 293.4$ K ±1.6%, yielding a freestream unit Reynolds number of 6.79 × 10^{7}/m ±4.8%. To avoid condensation shocks in the test section, the dew point of the flow was maintained below 244 K throughout the experiment.

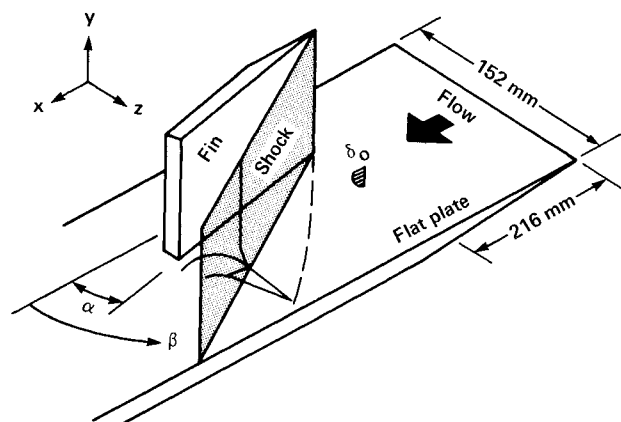As shown in Fig. 1, the geometry for the present experiment consists of a sharp unswept fin mounted on a flat plate, 495 mm long, which spanned the test section. The plate is fitted with both surface-pressure taps and surface thermocouples. Ninety-six surface-pressure taps are arranged in five concentric circular arcs about the fin leading-edge position. This arrangement was chosen to take advantage of the well-known quasiconical symmetry[1] of this class of swept interactions. An unswept-leading-edge fin shock generator mounted on the flat plate is positioned with its 10-deg sharp leading edge 216 mm from the plate leading edge and 26.2 mm from the tunnel sidewall. The fin is 76 mm high, 127 mm long, and 6.35 mm thick. The fin height of about $25\delta_0$ produces a semi-infinite, dimensionless swept interaction[1] over the entire span of the test section. A pneumatic fin-injection mechanism is used to vary the fin angle of attack with 0.1-deg accuracy.

Pitot-pressure surveys[11] along the flat-plate centerline and 38 mm to each side showed that the test boundary layer is two-dimensional, turbulent, and in equilibrium in the sense that it satisfies the combined law-of-the-wall/law-of-the-wake with constant wake strength parameter within the acceptable equilibrium range. The incoming boundary layer at $x = 216$ mm has $\delta_0 = 3.0$ mm, $\theta_0 = 0.16$ mm, and $Re_\theta = 11,160$. For the present study, c_f in the incoming boundary layer is predicted to be 1.2×10^{-3} according to the Van Driest II theory. Furthermore, $T_w/T_{aw} = 1.06 \pm 2.5\%$, so that the test boundary layer is almost adiabatic.

LISF Instrument and Data Acquisition

A schematic diagram of the LISF meter setup for the present experiment is shown in Fig. 2: the beam from a 5-mW linearly-polarized He-Ne laser (1) passes through a 50% neutral-density filter (2) and an iris diaphragm (3). The beam is then directed downward by a folding mirror (4), and focused by a focusing lens (5), passing through the Plexiglas ceiling window (6) of the wind tunnel to form a spot of about 400-μm diam on the flat plate. The beam angle of incidence with respect to the plate is kept to about 1 deg. During wind-tunnel runs, a thin film of $\nu = 500$ cS Dow-Corning "200" silicone oil (7) applied to a local region of the flat plate is sheared by the τ_w distribution of the shock/boundary-layer interaction due to the fin (8). The incident laser beam is then reflected by both the surface of the oil film and the polished metal surface beneath it. This produces interference between the two reflected laser beams, which are directed out of the wind tunnel through the Plexiglas ceiling window. The reflected beams pass through the lens (5), which now serves as a collecting lens. Then they are intercepted by two first-surface aiming mirrors, (9) and (10), and are directed through a ground glass (11) into a housing (12), which contains a 6328 Å filter and a photodiode.

The photodiode senses a time-dependent light intensity due to the constructive and destructive interference between the two reflected beams from the oil film and the polished test surface. The photodiode output [(13) in Fig. 2] is then raised to a
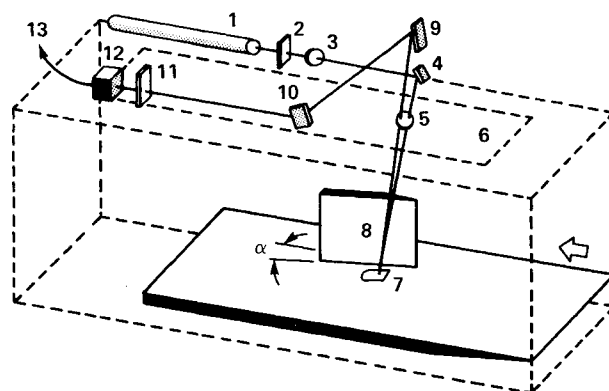

Fig. 1   Diagram of test geometry.
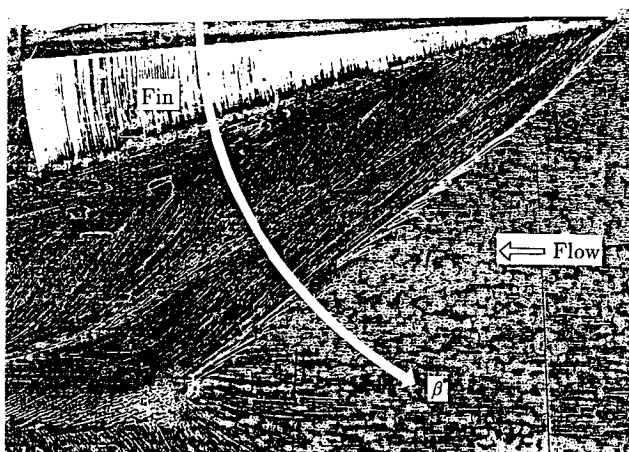

Fig. 2   Diagram of LISF instrument.

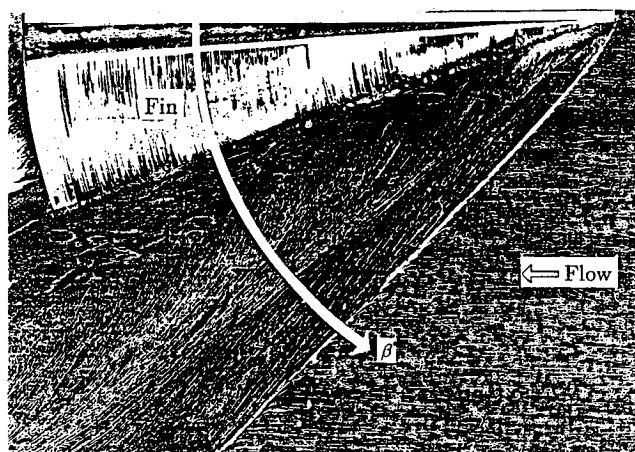Fig. 3   Surface flow pattern, $M_\infty = 4$, $\alpha = 16$ deg.

Fig. 4   Surface flow pattern, $M_\infty = 4$, $\alpha = 20$ deg.

level of around 8 V by an operational amplifier, low-pass filtered with a 10-Hz cutoff to remove high-frequency noise, and digitally recorded. For the current experiment, seven other channels of data are also recorded: p_0, T_0, two p_w signals, and three T_w signals. These eight data channels are simultaneously sampled by a multiplexer, digitized by a microcomputer-controlled A/D converter, and stored in the computer memory. For present purposes, two different data acquisition rates were used. A 20-Hz data acquisition rate was initially chosen for low-shear regions of the flow, yielding at least 20 points per interference fringe. However, the requirement for better accuracy in high-shear regions led to an increase of the data rate to 50 Hz. During experiments, the photodiode output was also monitored in real time on a stripchart recorder.

The entire LISF instrument is pedestal-mounted on an optical breadboard independent of the wind tunnel itself. Traversing units supporting this breadboard allow the x-y-z adjustment of the LISF instrument to locate the laser-beam spot accurately on the test surface without adjusting individual optical components.

LISF Measurement Technique

Since this embodiment of the LISF meter makes only discrete pointwise measurements, surveying the entire "footprint" of an unknown three-dimensional flow could be a daunting chore. However, for dimensionless fin-generated shock/boundary-layer interactions, a considerable body of past research[1] has revealed an inherent quasiconical symmetry of the flow, which considerably simplifies this task. In such a case, only one "cut" through the interaction need be measured, since any other measurement outside the initial "inception zone" is observed to be similar when rendered in spherical coordinates about the virtual origin of the flow. We have

therefore chosen a single measurement arc on the flat plate, centered about the fin leading edge with $R = 88.9$ mm, along which to take LISF data. This was chosen midway between the pressure-tap arcs mentioned earlier in order to avoid their interference with the LISF measurement. Eleven individual data points were taken along this arc for each of the $\alpha = 16$ and 20 deg test cases.

For LISF measurements in three-dimensional flows it is necessary to know the directions of the local surface streamlines, since an accurate reading of the distance along such a streamline from the oil-film leading edge to the laser-beam spot is required. These local surface streamline directions are determined using a kerosene-lampblack surface flow visualization technique.[12] This method produces undistorted full-scale patterns of the mean surface streamlines by way of a dry-transfer process using matte acetate tape. Angular measurements of local mean-shear directions are thus possible with ± 2-deg accuracy. Such patterns were obtained for the $\alpha = 16$ and 20 deg fin test cases at $M_\infty = 4$, and are shown in Figs. 3 and 4, respectively. Also indicated in these figures is the measurement arc along which the LISF data were taken. Similar patterns at $\alpha = 10$ and 16 deg for $M_\infty = 3$ were previously shown in Ref. 10.

During LISF tests, a full-scale transparent overlay of the surface streamline pattern is used to identify the surface-flow direction corresponding to a given position of the laser-beam measuring spot. After applying an oil drop to the test surface, it is squeezed by a small glass flat to produce a thin oil film. An optical cathetometer with a dial-gauge (least count: 0.025 mm) aligned normal to the surface-flow direction is next used to measure the distance from the oil-film leading edge to the center of the focused laser-beam spot. This distance should be measured with an error less than $\pm 1\%$, since it directly affects the accuracy of c_f. We now use a Questar DR1 Telemicroscope in place of the cathetometer for a more accurate oil-film leading-edge distance measurement.
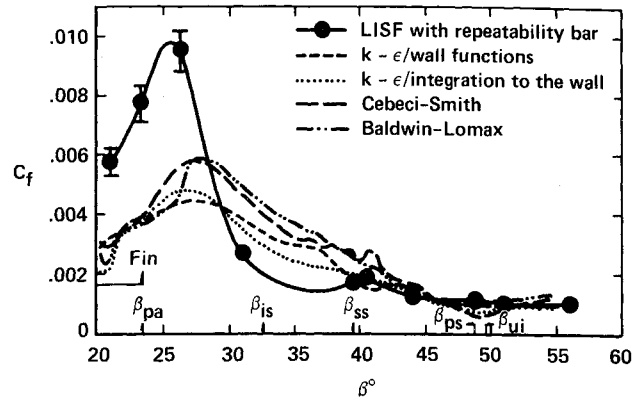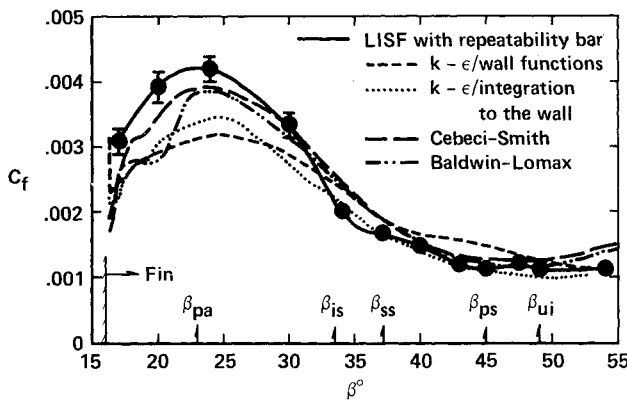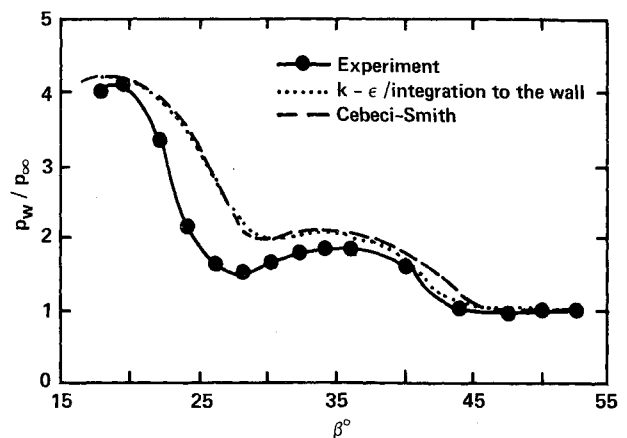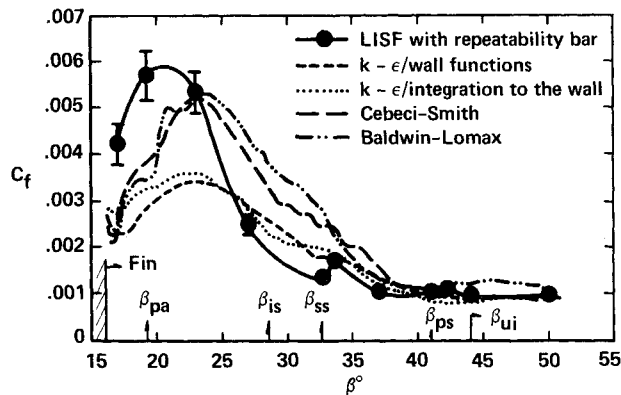
Data Reduction and Error Analysis

A detailed account of LISF data reduction procedures is given by Monson.[6] Furthermore, Kim and Settles[9,10] and Kim[13] thoroughly discussed the special features of LISF data reduction for compressible and high-shear flows. Thus, these procedures are not repeated in this paper.

The uncertainties in the flow quantities and other parameters connected with the LISF measurements have been cited in the previous sections. In all cases, these uncertainties are given as the mean value $\pm$ 2 standard deviations. However, the error bars in the plots of Figs. 5–8 show the repeatability of the data as only $\pm$ 1 standard deviation about the mean in the interest of clarity. No error bar at some LISF measurement location means that it is smaller than the symbol size.

Each measurement point within the two swept interactions studied here was repeated seven times in separate wind-tunnel runs. Chauvenet's criterion[14] was then applied once to each seven-point ensemble to discard, if necessary, a single bad point from the ensemble. In general, the resulting repeatability band varied from as little as $\pm 2\%$ upstream of the interaction to as much as $\pm 20\%$ at the location of the highest τ_w. It has been noted[9,10] that extremely high values of τ_w limit the number of usable fringes one may obtain, thus adversely affecting LISF data repeatability. In the current experiments, shear levels up to 1000 Pa were successfully measured by the LISF meter (using $\nu = 1000$ cS oil). This is almost twice the maximum τ_w value reached in our previous work.[10]

Computational Methods

The governing equations used to describe the flowfield are the compressible three-dimensional Navier-Stokes equations using mass-averaged variables in strong conservation form. These equations are listed in Ref. 15. Their restrictions include the calorically-perfect-gas assumption, the Sutherland viscosity law, and zero bulk viscosity. Four eddy-viscosity
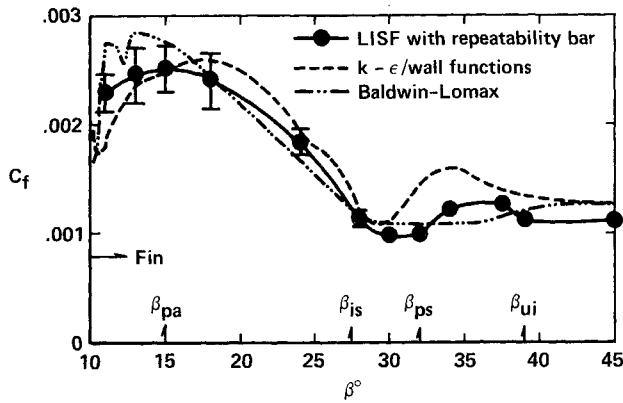
Fig. 5   Coefficient c_f vs β for $M_\infty = 3$, $\alpha = 10$ deg.

Fig. 6   Coefficient c_f vs β for $M_\infty = 3$, $\alpha = 16$ deg.

Fig. 7   Coefficient c_f vs β for $M_\infty = 4$, $\alpha = 16$ deg.

Fig. 8   Coefficient c_f vs β for $M_\infty = 4$, $\alpha = 20$ deg.

Fig. 9   Pressure data p_w/p_∞ vs β for $M_\infty = 4$, $\alpha = 16$ deg.
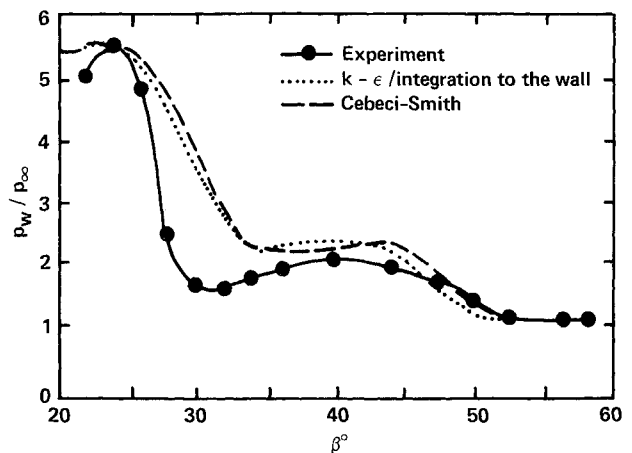
Fig. 10   Pressure data p_w/p_∞ vs β for $M_\infty = 4$, $\alpha = 20$ deg.

models are employed for turbulence closure: the algebraic models of Baldwin-Lomax[16] and Cebeci-Smith,[17] which are integrated to the wall, and a two-equation eddy-viscosity (k-ϵ) model with either wall-function boundary conditions[18] or integration to the wall using the Jones-Launder low-Reynolds-number terms.[19] Further details of the boundary conditions and algorithm used here are given by Knight et al.[20] and Horstman.[21]

The computational domain extends from a prescribed upstream boundary where an equilibrium turbulent boundary layer is generated (matching the experimental data) to a point well downstream of the interaction. Within this domain the grid was generated so as to take advantage of the experimentally-observed quasiconical flowfield. In the x-z (horizontal) plane the grid was developed using a family of rays originating from a virtual origin slightly upstream of the fin leading edge. Ahead of the interaction these rays were replaced by lines of constant z (spanwise direction). In the x (streamwise) direction, constant spacing was used. In the y (vertical) direction a variable spacing was used, concentrating most of the points

within the boundary layer. When integrating to the wall, the maximum value of y^+ for the first grid point was 0.1 in the interaction region. The resulting grid spacing in the x and z directions was approximately equal to $0.5\delta_0$. The total computational domain encompassed $64 \times 40 \times 64$ grid points in the x, y, and z directions, respectively.

Results and Discussion

Figures 9 and 10 show wall-pressure distributions at $M_\infty = 4$, $\alpha = 16$ and $\alpha = 20$ deg respectively. The pressure data are plotted vs the angle β measured from the fin leading edge (see Fig. 1), since the interaction is quasiconical. The data are compared with two computations using k-ϵ/integration to the wall and Cebeci-Smith turbulence models. The computed results predict the correct spanwise extents and peak values in both cases, but do not show the experimentally observed local

pressure minimum near $\beta = 27$ and 30 deg, respectively. This local pressure minimum occurs because of the high reversed velocity of the vortex, which dominates the flowfield.

Figure 5 shows the LISF skin-friction distribution measured in the $M_\infty = 3$, $\alpha = 10$ deg interaction. The c_f data are plotted vs the angle β. The data are compared with two computations using k-ϵ/wall-functions and Baldwin-Lomax turbulence models. Briefly, both computations reasonably predict the peak measured c_f level around $\beta = 15$ deg, as well as its decay with increasing β. However, the computation using the Baldwin-Lomax model fails to predict the observed initial increase in c_f near the beginning of the interaction, while the k-ϵ/wall-functions computation somewhat overpredicts this initial increase.

The measured c_f distribution for $M_\infty = 3$, $\alpha = 16$ deg is shown in Fig. 6. The data are compared with computations using four turbulence models described earlier. Briefly, the k-ϵ/wall-functions computation produces the worst prediction of the measured peak c_f at $\beta = 23$ deg. Overall, the Cebeci-Smith model is in best agreement with the data, though the distinction is not strong at this test condition.

The measured c_f distribution for $M_\infty = 4$, $\alpha = 16$ deg is shown in Fig. 7. The flat-plate c_f level ahead of the interaction is 0.00097, which agrees well with the value of 0.00099 obtained by Preston-tube. The overall c_f measurement accuracy at $\beta > \beta_{ss}$ is $\pm 3.2\%$. Figure 7 shows a slight peak in the measured c_f level between the upstream influence line ($\beta = 44$ deg) and the primary-separation line ($\beta = 41$ deg). As in the weaker interactions[10] of Figs. 5 and 6, this is believed to be due to the shearing-away of the lower portion of the incoming boundary layer by the swept pressure gradient of the flow. Low-momentum fluid is thus removed from the boundary layer, such that the velocity-gradient normal to the surface (and thus c_f) is increased.

Just ahead of the secondary-separation line ($\beta = 32.6$ deg) in Fig. 7, another local c_f peak is observed. This peak is clearly connected with the secondary-separation line (see Fig. 3), and is perhaps the first quantitative measurement yet obtained to indicate that there is actually something there. This peak is also observed by Preston-tube pressure measurement.[22] Unfortunately, not enough is known about the physics of this phenomenon to offer further insight at this time. Such a c_f peak is not observed in the weaker interactions of Figs. 5 and 6, even though a secondary-separation line is evident in the surface-flow patterns for both cases. This could be because the local resolution of the LISF measurement locations may not have been sufficient in the $M_\infty = 3$ interactions to reveal this feature.

Aft of the secondary-separation line in Fig. 7 there is a sharp increase in the measured c_f, reaching a maximum of almost six times the incoming c_f level near the primary flow-attachment line ($\beta = 19.2$ deg). This steep rise to a c_f peak can be explained in terms of the λ-shock structure[23] of the interaction, which causes the impingement of a high-speed jet upon the flat plate in the vicinity of the primary attachment line. This phenomenon is known to produce high τ_w, p_w, and heat transfer levels.[24] Recent visualizations of the structure of such swept interactions by conical shadowgraphy[25,26] show this jet impingement quite clearly, and also reveal a disturbance in the flowfield structure corresponding to the location of the secondary-separation line discussed earlier.

Figure 11 is a photo of an oil-film interference fringe pattern obtained in the $M_\infty = 4$, $\alpha = 16$ deg interaction. Such visible patterns provide quick qualitative indications of c_f distributions. To obtain such a pattern, several drops of oil are applied along the measurement arc and are squeezed by a glass flat as described earlier. In so doing, a thin oil film is created along the circular arc with a near-uniform initial thickness. During a wind-tunnel run, the interference fringe pattern forms naturally because of the shear distribution imposed by the flow. Thus, fringe spacing is generated depending on the shear level. It may be seen and photographed in white light.
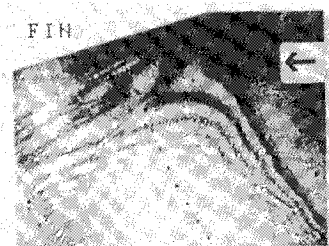

Fig. 11   Oil-film interference-fringe pattern, $M_\infty = 4$, $\alpha = 16$ deg.

The flow direction in Fig. 11 is from right to left. A strong fringe peak is clearly seen near the fin on the flat-plate surface. Two other small local peaks are also seen in the fringe pattern. These occur just ahead of the locations of the primary and secondary separation lines observed in the surface streamline pattern.

Comparing Figs. 7 and 11, the oil-film interference fringe pattern obtained at $M_\infty = 4$ and $\alpha = 16$ deg shows qualitatively the same trend as the measured c_f distribution. Thus, we may regard a fringe pattern such as Fig. 11 as being qualitatively indicative of the actual c_f distribution. Unfortunately, any quantitative analysis of such a pattern to yield c_f values directly is rendered impossible by the lack of knowledge of the complex shear-stress history of the surface streamlines arriving at fringe locations in the pattern. Nonetheless, visual inspection of such oil-film interference fringe patterns yields a valuable first glance at the c_f distribution, whence the detailed pointwise measurements of c_f using the LISF meter may be planned.

Figure 7 also shows the results of computed Navier-Stokes solutions using the four different turbulence models described earlier. These four computations are in reasonable agreement with the LISF data only up to the secondary-separation line. The computations using the Jones-Launder k-ϵ model and two different wall-treatment schemes (wall functions or integration to the wall) show similar results: they severely underpredict the measured peak c_f value by 40%. Initially, integration to the wall was thought to be a more adequate (and certainly more expensive) approach than wall functions for such a complex interacting flow, but no such distinction is supported by the c_f results of Fig. 7.

Computations using the algebraic Cebeci-Smith and Baldwin-Lomax turbulence models also show similar c_f trends in Fig. 7. However, they underpredict the measured peak c_f value by only 12%. It comes as an additional surprise that the simpler algebraic turbulence models actually outperform the more complex k-ϵ approach in this strongly-interacting separated flow. Finally, the Cebeci-Smith model is the only one that predicts the local c_f peak associated with the secondary-separation line.

The c_f distribution for the $M_\infty = 4$, $\alpha = 20$-deg case is shown in Fig. 8. The trend of c_f vs β is similar to that of the case just discussed. However, the local c_f peak between the upstream influence line ($\beta = 49.5$ deg) and the primary-separation line ($\beta = 48.8$ deg) and that just ahead of the secondary-separation line ($\beta = 39.5$ deg) are not so pronounced as in the previous case. Also, the peak c_f value is rather dramatic in the strong-interaction case of Fig. 8, being almost an order of magnitude higher than the incoming free-stream c_f level. Note, in this case, that the peak c_f occurs about 3 deg forward of the primary attachment line at $\beta = 23.3$ deg.

Comparative computations are also shown in Fig. 8, with results similar to those of Fig. 7. Though the predicted peak c_f is slightly higher here than for the $M_\infty = 4$, $\alpha = 16$ deg case, it does not keep pace with the rapidly rising peak in the measured c_f with increasing interaction strength. The k-ϵ computations underpredict the measured peak c_f by 50%, again with little distinction between integration to the wall and wall functions. As in the previous $M_\infty = 4$, $\alpha = 16$ deg case, the

Cebeci-Smith model is the only one to predict the local c_f peak just ahead of the secondary-separation line. The predicted peak c_f values using Cebeci-Smith and Baldwin-Lomax models are slightly higher than those of the k-ϵ model, but still 40% below the measured c_f peak. All predictions except k-ϵ/wall functions show an initial drop in c_f near the primary-separation line, where the data show a slight increase.

The trends of both the LISF data and computations with increasing interaction strength may be seen most clearly by plotting $c_{f_{peak}}/c_{f_\infty}$ vs the pressure ratio (p_2/p_1) across the undisturbed "inviscid" fin shock wave, as shown in Fig. 12. For clarity, only the computational solutions using k-ϵ/wall functions and Cebeci-Smith models are shown in this figure. It can be seen clearly that the measured peak c_f values rise in a well-behaved but nonlinear fashion with increasing interaction strength, such that it fails progressively as the interaction strength is increased. The prediction using the Cebeci-Smith model does a better job for weak and moderate-strength interactions, but then falls off dramatically between $M_\infty = 4$, $\alpha = 16$ and 20 deg.

Figures 13 and 14 show the angles of the surface skin-friction lines, ϕ, plotted against β along the measurement arcs of the present $M_\infty = 4$, $\alpha = 16$ and 20 deg interactions, respectively. The solid circles denote experimental points extracted from the surface streamline patterns shown previously in Figs. 3 and 4. The error bar represents the overall accuracy of ϕ measurements. The local minima in the measured angles ϕ at $\beta = 32.6$ and 39.5 deg, respectively, in Figs. 13 and 14 represent the secondary-separation lines that are clearly seen in the corresponding surface streamline patterns.

The comparative results of the four different Navier-Stokes solutions are also shown in Figs. 13 and 14. In no case do the computations predict the measured surface streamline angles correctly over the entire interaction. However, the k-ϵ/wall-functions solution clearly does the poorest job in comparison with the data, grossly underpredicting the extent of the

observed upstream influence. The other three computations are better at this with only small differences among them. They all overpredict ϕ near the secondary-separation lines and underpredict ϕ between the inviscid shock locations and the primary attachment lines of the two interactions. Note especially that integration to the wall appears to have solved the nagging problem of underprediction of the upstream influence of such interactions, which occurs here and in several previous studies where k-ϵ/wall-function turbulence modeling was used. Of the four computational solutions shown, k-ϵ/ integration to the wall appears to do the best overall job of predicting surface streamline angles in both interactions shown in Figs. 13 and 14.

Next, computed eddy-viscosity distributions are plotted vs y and compared in Fig. 15 for the $M_\infty = 4$, $\alpha = 16$ deg interaction at $\beta = 23$ deg, which is near the peak value of the computed c_f. This figure clearly shows why the algebraic eddy-viscosity models predict the higher values of peak skin friction: both algebraic models produce higher μ_t values throughout the flowfield than does the k-ϵ approach. The Baldwin-Lomax model makes the eddy viscosity proportional to vorticity, resulting in high values far above the wall due to the vortical structure of the separated flowfield. Also note that the two k-ϵ solutions show different values of eddy viscosity in the flowfield while predicting similar values of skin friction; this is because the wall-function treatment uses an algebraic equation rather than the actual velocity derivative at the wall in calculating c_f.

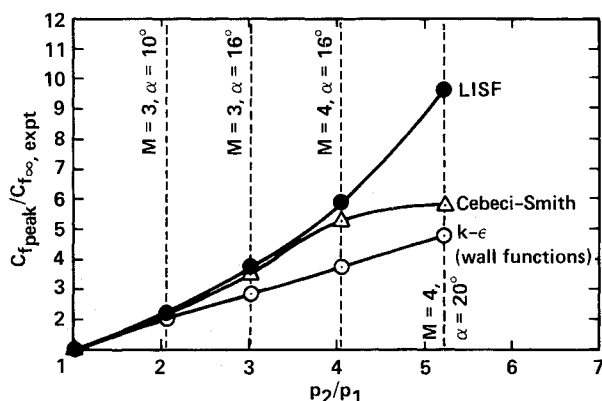Fig. 14   Angle ϕ vs β for $M_\infty = 4$, $\alpha = 20$ deg.

Fig. 12   Peak skin-friction coefficient vs pressure ratio across inviscid shock wave.
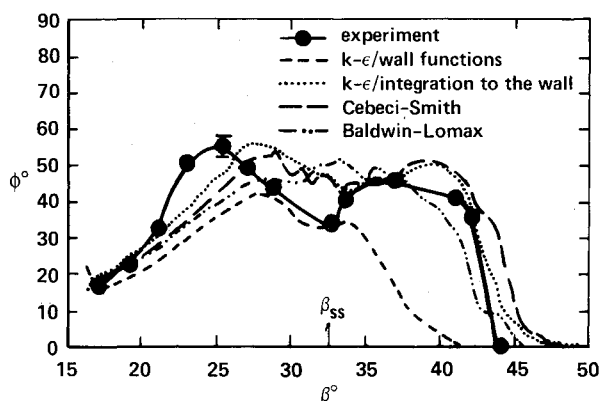
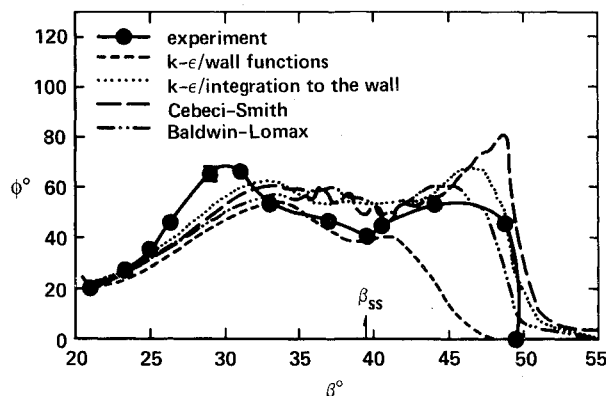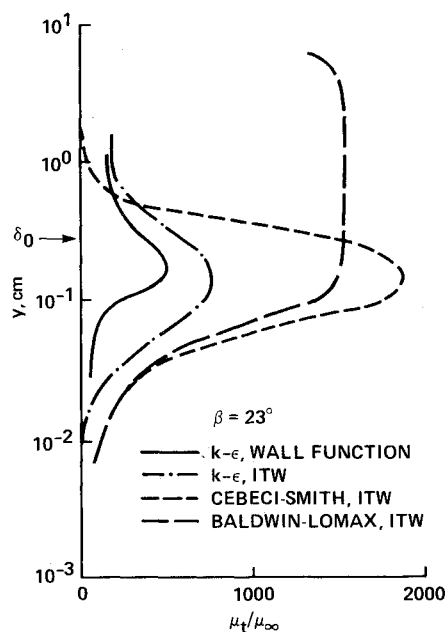Fig. 13   Angle ϕ vs β for $M_\infty = 4$, $\alpha = 16$ deg.

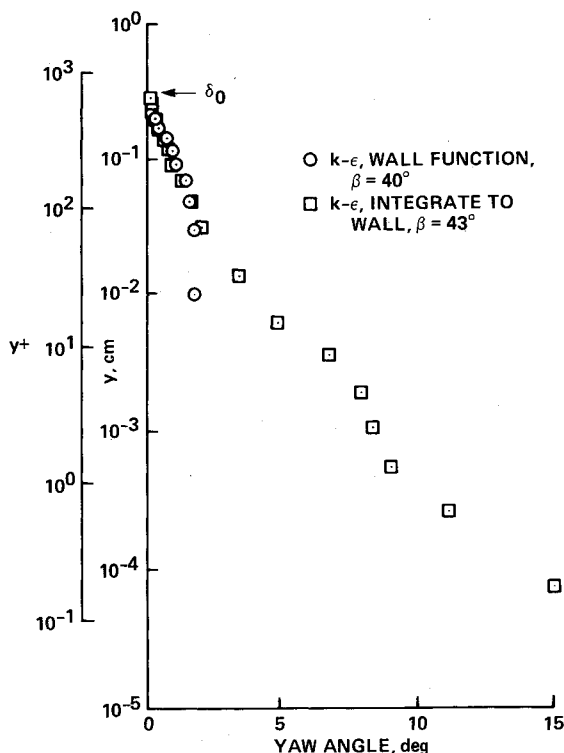Fig. 15   Distributions μ_t/μ_∞ vs y for $M_\infty = 4$, $\alpha = 16$ deg.

Fig. 16 Yaw angle vs y for $M_\infty = 4$, $\alpha = 16$ deg.

5) The computational prediction of peak skin friction using algebraic turbulence models achieves an improvement due to their production of higher eddy-viscosity levels; however, they still fail for the strongest interactions studied.

6) This failure of computational skin-friction predictions is manifested in the aft half of the interaction zone, where the peak c_f level is underpredicted by as much as 50%.

7) The wall-treatment scheme (wall functions vs integration to the wall) used in the k-ϵ turbulence model has a secondary effect on the prediction of skin friction, but an important effect on the prediction of measured surface-streamline patterns and the extent of upstream influence. In the latter case, the k-ϵ/integration-to-the-wall turbulence model produces the best prediction.

8) The LISF technique has been successfully applied up to a wall shear-stress level of 1000 Pa in this study.

In Figs. 13 and 14 it was shown that the predicted upstream influence changes significantly depending on the use of wall functions or integration to the wall. This is due to the implicit assumption, in the wall-functions case, that there is no flow turning below the second grid point away from the wall. Two examples of computed flow yaw-angle profiles shown in Fig. 16 illustrate this point (yaw angle is defined as the direction of the velocity vector in the x-z plane). In this figure the computed yaw angle at each grid point is plotted vs y and y^+ for the Mach 4, $\alpha = 16$ deg interaction. The locations of these profiles are $\beta = 40$ deg (wall functions) and $\beta = 43$ deg (integration to the wall), both near the upstream-influence line of the interaction. It is seen in Fig. 16 that the predicted yaw angle increases significantly in the region very close to the wall, well below the minimum-height grid point employed by the wall-functions treatment. This increases the upstream influence and eventually affects the entire flowfield. Thus, any future wall-function computations for this class of swept interactions should definitely allow for additional turning below the first two grid points. (Work is in progress to accomplish this.)

Conclusions

A joint experimental and computational study of skin friction in weak-to-strong swept shock wave/turbulent boundary-layer interactions at $M_\infty = 3$ and 4 has been carried out. The significant conclusions of this study are as follows:

1) A strong peak in measured skin friction occurs in the vicinity of the primary flow attachment line in the swept interactions.

2) This skin-friction peak rises monotonically with increasing interaction strength, reaching a value an order of magnitude higher than the incoming flat-plate skin-friction level for the strongest interaction measured here.

3) A small local skin-friction peak is found just ahead of the surface-flow feature known as the secondary-separation line.

4) Although skin-friction prediction using a k-ϵ/wall-functions turbulence model in these flows is adequate for the weakest cases studied, it fails systematically with increasing interaction strength.

References

[1]Settles, G. S., and Dolling, D. S., "Swept Shock Wave/Boundary-Layer Interactions," *Tactical Missile Aerodynamics*, edited by M. Hemsch and J. Nielsen, Vol. 104, Progress in Astronautics and Aeronautics, AIAA, Washington, DC, 1986, pp. 297–379.

[2]Tanner, L. H., and Blows, L. G., "A Study of the Motion of Oil Films on Surfaces in Air Flows, with Application to the Measurement of Skin Friction," *Journal of Physics E: Scientific Instruments*, Vol. 9, No. 3, 1976, pp. 194–202.

[3]Tanner, L. H., and Kulkarni, V. G., "The Viscosity Balance Method of Skin Friction Measurement: Further Developments Including Applications to Three-Dimensional Flow," *Journal of Physics E: Scientific Instruments*, Vol. 9, No. 12, 1976, pp. 1114–1121.

[4]Tanner, L. H., "A Skin Friction Meter, Using the Viscosity Balance Principle, Suitable for Use with Flat or Curved Metal Surfaces," *Journal of Physics E: Scientific Instruments*, Vol. 10, No. 3, 1977, pp. 278–284.

[5]Monson, D. J., and Higuchi, H., "Skin Friction Measurements by a Dual-Laser-Beam Interferometer Technique," *AIAA Journal*, Vol. 19, No. 6, 1981, pp. 739–744.

[6]Monson, D. J., "A Nonintrusive Laser Interferometer Method for Measurement of Skin Friction," *Experiments in Fluids*, Vol. 1, No. 1, 1983, pp. 15–22.

[7]Monson, D. J., "A Laser Interferometer for Measuring Skin Friction in Three-Dimensional Flows," *AIAA Journal*, Vol. 22, No. 4, 1984, pp. 557–559.

[8]Westphal, R. V., Bachalo, W. D., and Houser, M. H., "Improved Skin Friction Interferometer," NASA TM 88216, March 1986.

[9]Kim, K.-S., and Settles, G. S., "Skin Friction Measurements by Laser Interferometry," *A Survey of Measurements and Measurement Techniques in Rapidly Distorted Compressible Turbulent Boundary Layers*, edited by H. H. Fernholz, A. J. Smits, and J.-P. Dussauge, AGARDograph 315, Nov. 1988, pp. 4.1–4.8.

[10]Kim, K.-S., and Settles, G. S., "Skin Friction Measurements by Laser Interferometry in Swept Shock/Boundary-Layer Interactions," *AIAA Journal*, Vol. 28, No. 1, 1990, pp. 133–139.

[11]Lu, F. K., "Mach Number Effects on Fin-Generated Shock-Wave Boundary-Layer Interactions," Ph.D. Dissertation, Mechanical Engineering Dept., Pennsylvania State Univ., University Park, PA, 1988.

[12]Settles, G. S., Metwally, O. M., Hsu, J. C., and Lu, F. K., "Visualization of High-Speed Flows at the Penn State Gas Dynamics Laboratory," *Proceedings of the 1988 International Conference on Applications of Lasers and Electro-Optics*, Laser Inst. of America, Toledo, OH, Vol. 67, 1988, pp. 95–101.

[13]Kim, K.-S., "Skin Friction Measurements by Laser Interferometry in Supersonic Flows," Ph.D. Dissertation, Mechanical Engineering Dept., Pennsylvania State Univ., University Park, PA, 1989.

[14]Holman, J. P., *Experimental Methods for Engineers*, 2nd ed., McGraw-Hill, New York, 1971, pp. 55–57.

[15]Settles, G. S., Horstmann, C. C., and McKenzie, T. M.,

"Flowfield Scaling of a Swept Compression Corner Interaction—A Comparison of Experiment and Computation," AIAA Paper 84-0096, Jan. 1984.

[16]Baldwin, B. S., and Lomax, H., "Thin Layer Approximation and Algebraic Model for Separated Turbulent Flows," AIAA Paper 78-0257, Jan. 1978.

[17]Cebeci, T., and Smith, A. M. O., *Analysis of Turbulent Boundary Layers*, Academic, New York, 1974.

[18]Viegas, J. R., Rubesin, M. W., and Horstman, C. C., "On the Use of Wall Functions as Boundary Conditions for Two-Dimensional Separated Compressible Flows," AIAA Paper 85-0180, Jan. 1985.

[19]Jones, W. P., and Launder, B. E., "The Prediction of Laminarization with a Two-Equation Model of Turbulence," *International Journal of Heat and Mass Transfer*, Vol. 15, Feb. 1972, pp. 301–314.

[20]Knight, D. D., Horstman, C. C., Shapey, B., and Bogdonoff, S. M., "Structure of Supersonic Turbulent Flow Past a Sharp Fin," *AIAA Journal*, Vol. 25, No. 10, 1987, pp. 1331–1337.

[21]Horstman, C. C., "Computation of Sharp-Fin-Induced Shock Wave/Turbulent Boundary-Layer Interactions, *AIAA Journal,* Vol. 24, No. 9, 1986, pp. 1433–1440.

[22]Kim, K.-S., Lee, Y., and Settles, G. S., "Laser Interferometer/Preston Tube Skin Friction Comparison in Swept Shock/Boundary Layer Interactions," *AIAA Journal*, Vol. 29, No. 6, 1991, pp. 1007–1009.

[23]Lu, F. K., and Settles, G. S., "Structure of Fin-Shock/Boundary-Layer Interactions by Laser Light-Screen Visualization," AIAA Paper 88-3801, July 1988.

[24]Edney, B. E., "Anomalous Heat Transfer and Pressure Distributions on Blunt Bodies at Hypersonic Speeds in the Presence of an Impinging Shock," Aeronautical Research Inst. of Sweden, FFA Rept. 115, Stockholm, Feb. 1968.

[25]Alvi, F. S., and Settles, G. S., "A Parametric Study of Swept Shock Wave/Turbulent Boundary-Layer Interaction Structure Using Conical Shadowgraphy," AIAA Paper 90-1644, July 1990.

[26]Alvi, F. S., and Settles, G. S., "A Physical Model of the Swept Shock Wave/Turbulent Boundary-Layer Interaction Flowfield," AIAA Paper 91-1768, June 1991.